International Journal of Solids and Structures 305 (2024) 113040

Contents lists available at ScienceDirect

International Journal of Solids and Structures

journal homepage: www.elsevier.com/locate/ijsolstr

A multi-step auxetic metamaterial with instability regulation

Penghui Yu [a], Peijie Zhang [a], Qingxiang Ji [a], Fan Yang [a], Xiaojun Tan [b], Xueyan Chen [a,*], Huifeng Tan [a,*], Vincent Laude [c], Muamer Kadic [c,*]

[a] National Key Laboratory of Science and Technology on Advanced Composites in Special Environments, Harbin Institute of Technology, 92 Xidazhi Street, Harbin, 150001, PR China
[b] School of Civil Aviation, Northwestern Polytechnical University, Xi'an 710072, PR China
[c] Université de Franche-Comté, CNRS, Institut FEMTO-ST, 25000 Besançon, France

ARTICLE INFO

Keywords:
Auxetics
Mechanical metamaterial
Lightweight structure
Multi-step deformation
Tailored stability

ABSTRACT

A stable deformation mode is highly desired for mechanical metamaterials, especially when coupled with a negative Poisson's ratio. However, such metamaterials often face challenges in terms of scalability toward large deformation or strain. In response, we propose a multi-step hierarchical auxetic metamaterial design paradigm, incorporating a series of incrementally scaled-down structures with same scale factor α into a re-entrant framework. This design enables instability regulation and multi-step deformation capabilities while preserving auxetic behavior, even under significant strain. Such multi-step metamaterials exhibit excellent properties, including tailored multi-phase compression modulus and strength, along with an enhanced energy absorption capacity that is as large as 2.1 times that of the original auxetic metamaterial. Experiments and simulations demonstrate that the deformation mechanism and compression response of the proposed multi-step auxetics are strongly influenced by the reduction factor and the order of the inner structure. A particularly intriguing observation is that the incorporation of embedded microstructures can restore stable deformation, even in the presence of significant initial instability, particularly with a reduction factor of 1/5. At high relative density, its specific energy absorption stands out favorably compared to other configurations, highlighting the success of the recoverable buckling mechanism. This work paves the way for designing multi-step mechanical metamaterials for use in impact resistance and body protection.

1. Introduction

Mechanical metamaterials, with their meticulously engineered periodic microstructures, display an extensive array of mechanical properties, including programmable deformations (Coulais et al., 2018; Florijn et al., 2014; Coulais et al., 2017; Gao et al., 2023), controlled Poisson's ratio (Bückmann et al., 2014, 2012; Chen et al., 2020b; Dudek et al., 2023a; Wang et al., 2022), high specific stiffness (Chen et al., 2020a; Han et al., 2015; Chen et al., 2022a), high specific strength (Berger et al., 2017; Tancogne-Dejean et al., 2018), high energy absorption (Chen et al., 2022b; Zhang et al., 2023; Jiang et al., 2022a), and reusable shock-absorbing capacity (Zhu et al., 2019; Frenzel et al., 2016). These mechanical properties are primarily influenced by structural topology, geometrical parameters, and the inherent characteristics of base materials (Yang and Ma, 2020a; Chen and Tan, 2018; Jang et al., 2013; Zheng et al., 2014).

Auxetics are a distinctive class of mechanical metamaterials characterized by a negative Poisson's ratio, which contract (expand) transversely when compressed (stretched) longitudinally. This unconventional behavior provides them with enhanced mechanical properties (Ren et al., 2018b; Luo et al., 2021), including shear and indentation resistance (Wang et al., 2017; Evans and Alderson, 2000), fracture toughness (Choi and Lakes, 1996), energy absorption capabilities (Wang et al., 2016, 2018), and wave propagation characteristics (Frenzel et al., 2017, 2019), when compared to mechanical metamaterials with a positive Poisson's ratio. Auxetic mechanical materials thus have garnered significant interest across diverse engineering disciplines, spanning civil and military sectors (Ren et al., 2018a), automotive engineering (Jiang et al., 2023), aerospace devices (Vocke et al., 2011; Wagner et al., 2019), medical implants (Huang et al., 2022), flexible electronics (Jiang et al., 2018), and more.

Pioneering this domain, Lakes introduced a 3D artificial auxetic foam where the ribs of each cell were designed to protrude inward permanently (Lakes, 1987). Later, Evans et al. defined the notion of auxeticity (Evans, 1991). Grima et al. expanded the auxetic materials repertoire by incorporating a mechanism composed of rotating rigid units, encompassing rotating squares (Grima and Evans, 2000; Grima et al., 2000), rectangles (Grima et al., 2004), triangles (Grima

* Corresponding authors.
E-mail addresses: chenxueyan@hit.edu.cn (X. Chen), tanhf@hit.edu.cn (H. Tan), muamer.kadic@univ-fcomte.fr (M. Kadic).

https://doi.org/10.1016/j.ijsolstr.2024.113040
Received 23 April 2024; Received in revised form 18 August 2024; Accepted 21 August 2024
Available online 2 September 2024

and Evans, 2006), and variously sized squares and rectangles (Grima et al., 2011). Since then, a myriad of auxetic materials has been conceived, employing diverse deformation mechanisms such as re-entrant structures (Gibson, 2003; Evans et al., 1994; Yang and Ma, 2020b), chiral structures (Lakes, 1991; Prall and Lakes, 1997; Ha et al., 2016), rotating polygon structures (Dudek et al., 2023a,b), perforated plate structures (Grima and Gatt, 2010; Grima et al., 2016), and other structures (Babaee et al., 2013; Smith et al., 2000). Recent breakthroughs in additive manufacturing allow for the creation of auxetic mechanical materials across multiple length scales employing a diverse range of base materials (Yuan et al., 2017; Bückmann et al., 2014, 2012).

Re-entrant structures hold a pivotal position within the auxetic family. The earliest example of 2D re-entrant honeycombs, achieved by incorporating a negative angle into the inclined member of a standard honeycomb structure, was introduced by Gibson et al. in 1982 (Gibson, 2003). Building on this foundation, subsequent research delved into the elastic constants of these structures, analyzing honeycomb cell deformations like flexure, stretching, and hinging (Masters and Evans, 1996). A noteworthy theoretical method was proposed, predicated on comparing strain energies at both the macro and micro scales, aiming to predict the effective properties of 2D re-entrant structures (Berinskii, 2016). For minimizing stress concentration around junctions, dynamic in-plane responses and multi-objective optimization of re-entrant structures, shaped by a sinusoidal curve, were obtained (Xu et al., 2021). By merging the re-entrant honeycomb design with hexagonal patterns, a new hybrid honeycomb structure was discerned. This structure boasts augmented stiffness, adjustable auxeticity, and exhibits negative thermal expansion (Peng and Bargmann, 2021). Additionally, Zhang et al. conducted a comprehensive study on the post-yield behavior of re-entrant hexagonal honeycombs under tension, using both analytical and numerical approaches (Zhang et al., 2018).

Generally, at low relative densities, these metamaterials exhibit global instability when subjected to large deformations, which in turn affects their mechanical properties (Niknam and Akbarzadeh, 2018; Wu et al., 2021; Viard et al., 2020; Li et al., 2021a). To address this challenge, numerous scholars have embarked on structural optimization designs rooted in the traditional concave structure with a negative Poisson's ratio. Innovations such as the inclusion of embedded microstructures (Cheng et al., 2022; Zhang et al., 2022) and the development of hierarchical designs (Jiang et al., 2020; Feng et al., 2022) have been explored to fortify their mechanical response. Nonetheless, these strategies introduce new complications, including increased structural mass and potential shifts from the foundational negative Poisson's ratio attributes of the material. Consequently, there is a pressing demand to devise a novel optimization approach that not only bolsters the nonlinear stability of re-entrant auxetic structures but also amplifies their energy absorption capabilities.

Multi-step deformation structures can impart unique and significant mechanical properties. Coulais et al. introduced a metamaterial capable of multi-step deformation, achieved via structural reconfiguration guided by a rotating mechanism, thereby negating the need for external sensing and control (Coulais et al., 2018). This underlying mechanism can also serve as a foundation for designing other multi-step metamaterials (Li et al., 2021b; Lu et al., 2022; Hyatt and Harne, 2022). Building upon this idea, Meng et al. introduced an innovative multi-step deformation structure that seamlessly combines sequential cell deformation with Euler buckling (Meng et al., 2020). In a different study, Jiang et al. examined the dual plateau characteristics of the re-entrant auxetic structure in its concave orientation (Jiang et al., 2022b). Meanwhile, Dudek et al. presented a micro-scale mechanical metamaterial featuring tunable extreme auxeticity and phononic band gaps, facilitated by structural reconfiguration (Dudek et al., 2023b). Collectively, multi-step deformation mechanisms demonstrate remarkable potential in the realm of deformation control.

Hierarchical design strategies have been widely employed in the creation of metamaterials for shape morphing (Dudek et al., 2022) and programming mechanical properties (Li et al., 2021b). Stemming from these insights, we propose in this work a novel class of multi-step hierarchical re-entrant auxetic metamaterial, integrated with microstructures of varying reduction ratios, specifically designed for energy absorption and instability regulation. The effects of geometrical parameters on the effective mechanical properties are analyzed using numerical simulations and experiments. Results show that the proposed structure not only offers modifiable multi-step deformation capabilities but also spans a broad range of auxetic behaviors. A particularly intriguing observation is that the introduction of embedded microstructures can also effectively control the global instability phenomenon that occurs in conventional re-entrant auxetic materials during the compression process without changing the structural mass and negative Poisson's ratio characteristics. Thus, the problem of reduced utilization due to structural instability can be avoided, and the energy-absorbing effect of the structure can be enhanced. Compared to the conventional re-entrant auxetic materials, the designed metamaterials have a specific energy absorption about 2.1 times as large.

2. Metamaterial design

We first outline a comprehensive design strategy that involves embedding a series of incrementally scaled-down structures into a 2D auxetic re-entrant framework (Fig. 1a and b). This approach aims to achieve controlled multi-step deformation behavior while also managing instabilities.

2.1. Design strategy

The design is based on a 2D re-entrant sinusoidal auxetic structure. Initially, it undergoes contraction by a factor of α to produce a primary microstructure. Then, two primary microstructures are embedded at the top and bottom of the original unit cell to form a second-order deformation structure. Subsequently, the primary microstructures are further contracted by the same factor and embedded within inner layers to create a third-order deformation structure. The core mechanism in this study involves converting the overall load into multiple deformation paths through sequential layer deformation within the unit cell (Fig. 1c). To demonstrate the general deformation mechanism, we subject numerically mechanical metamaterials consisting of 2×2 units to uniaxial compression under periodic boundary conditions (Fig. 1d). In terms of geometry, the embedding of the internal microstructure initiates deformation through the outer layer of the unit cell during the compression process. As the outer layer of the unit cell comes into contact with the internal microstructure, it drives the inner microstructure to deform (Fig. 1e), resulting in a multi-step deformation mechanism. Note that, in principle, the proposed design concept can be further extended to create metamaterials with n-step deformation.

Nonlinear stability is another significant concern in mechanical metamaterial. Conventionally, for first-order auxetics with low relative density, deformation behaviors at large strains are often unstable and thus need to be controlled (Fig. 1f). Unlike first-order auxetics, which typically buckle under axial compression, second-order auxetics, along with their embedding structures, have the capability to transform from an unstable stage to a stable stage (Fig. 1f). Certainly, the deformation path can also be carefully tailored to suppress or even avoid buckling behavior. Here, we numerically investigate the effects of reduction factor α and relative density $\overline{\rho}$ on the desired deformation mode. Utilizing 3×5 numerical models, we specially explore geometrical parameters ranging from α=0 to 0.4 and $\overline{\rho}$ from 0.05 to 0.3 (Fig. 1g). When α is constrained to values no greater than 0.1, the size of the embedded micro-structure results in an insufficient impact on regulating instability. In this scenario, the deformation modes of auxetics are predominantly governed by buckling. Upon increasing α to 0.2 and maintaining $\overline{\rho}$ within the confines of 0.1, the embedded micro-structures, characterized by thin thicknesses, contribute a low

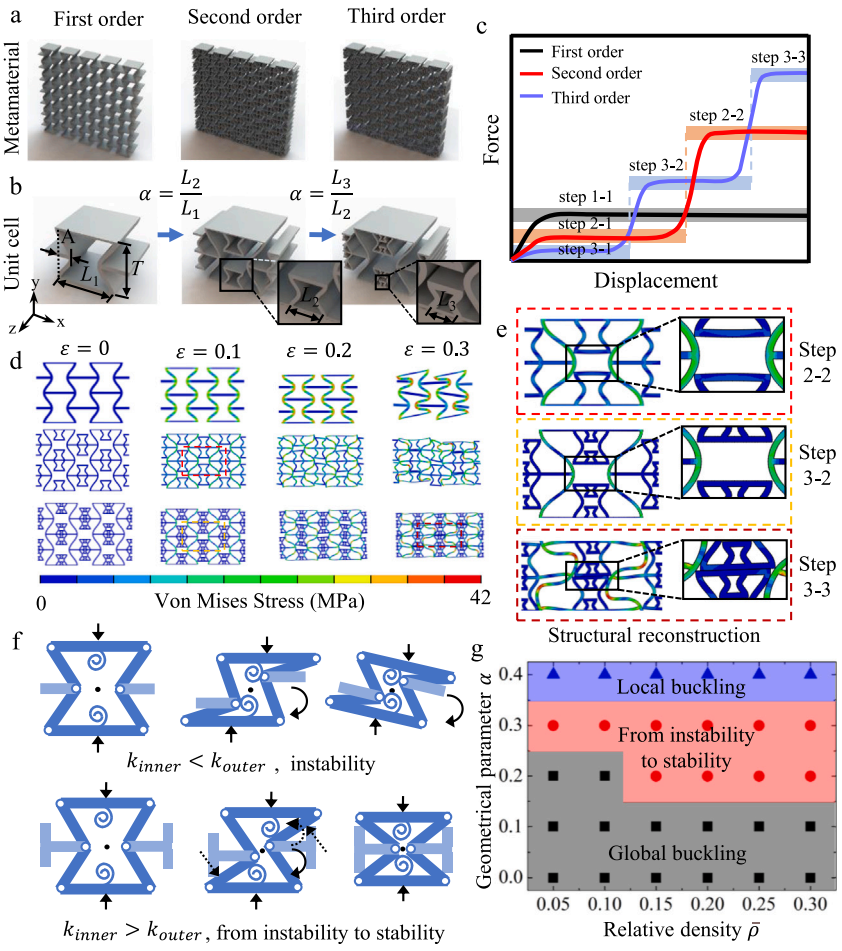

Fig. 1. Design concepts of multi-step auxetic metamaterials. Schematics of (a) the first-order conventional auxetic metamaterial, the high-order optimal multi-step auxetic metamaterials, and (b) their corresponding representative unit cells. (c) Force–displacement curves for the auxetic materials show the multi-step mechanical response. (d) Uniaxial compression simulations for the auxetic materials with periodic boundary conditions applied, (e) accompanied by zoom-in views of structural reconstructions within these multi-step auxetic materials under a specific applied strain, illustrate the deformation mechanism. (f) Conventional buckling mechanism is shown versus the unusual instability transition mechanism of multi-step auxetics. In this representation, the inner scaled-down amended structures are symbolized as simplified spirals. (g) The deformation modes of second-order auxetics vary with relative densities and reduction ratio, exhibiting three types: destabilization, recovery after destabilization, and destabilization after stabilization. The geometrical parameter α and relative density $\bar{\rho}$ are defined in the text, Section 2.1.

equivalent stiffness. Consequently, they prove ineffective in resisting the rotational deformation of the outer structure, and the deformation rule persists unchanged. However, a noteworthy transformation occurs when α is further elevated to 0.3 or when $\bar{\rho}$ exceeds 0.1. Above these thresholds, the embedded micro-structures exhibit heightened strength, effectively countering the rotational deformation of the outer structure. Subsequently, the overall structure undergoes a pronounced recovery, gradually returning to a stable stage after experiencing nonlinear instability. This signifies a critical transition where the embedded micro-structures become robust enough to decisively influence the structural response. At an α value of 0.4, the embedded microstructures assume a larger size and undergo reconstruction before the structure experiences destabilization. The stiffness of the inner scaled-down amended structure is larger than that of the outer layer of the unit cell, and the sufficiently large stiffness prevents the destabilization process of the structure. This preemptive reconstruction serves to stabilize the deformation at the initial stage, mitigating the destabilization process. Nevertheless, as compression continues, it gradually becomes destabilized at a later stage. These mechanisms enable the structure to withstand higher loads and significantly mitigates the risk of the original re-entrant auxetic structure experiencing instability buckling during compression. For the third-order structure, the dependence of the deformation modes on the relative densities and the reduction ratio were almost the same as for the second-order structure until the second reconfiguration. In contrast, after the third-order structure underwent second reconfiguration, the structures were rapidly destabilized global, which were different from the nearly stable deformation pattern of the second-order structures in the later stages of deformation. Consequently, the designed structures can serve as a stable energy-absorbing element.

2.2. Relative density

Figure S1 illustrates the geometry of the first-order auxetic unit cell along with its associated geometric parameters. The first-order re-entrant auxetic structure exhibits a sinusoidal curve shape on the side of the unit cell with the following expression:

$$y = A\cos\left(\frac{2\pi}{T}x\right). \tag{1}$$

The unit cell dimensions in the x and y directions are:

$$L_x = 4(L - A),\ L_y = T, \tag{2}$$

where A represents the amplitude of the sine curve, L corresponds to half the length of the horizontal part of the single cell, and T stands for the period of the sine curve. The unit cell size in the z direction is denoted as L_z, and the layer thickness is represented by t.

Relative density $\bar{\rho}$ is a crucial factor in mechanical metamaterials, primarily used to manage their mass. It is defined as the ratio of the

actual volume occupied by the mechanical metamaterials to the volume of the overall mechanical metamaterials. The relative density of the first-order auxetic metamaterial, determined by the ratio of the solid area of the structural cell (A_s) to its total cross-sectional area (A_{total}), can be expressed as:

$$\overline{\rho}_1 = \frac{A_s}{A_{total}} = \frac{(S+2L)t - t^2}{2T(L-A)}, \tag{3}$$

where the length of the sinusoidal part of the side of the unit cell is $S = \int_{-\frac{T}{2}}^{\frac{T}{2}} \sqrt{1 + (\frac{2\pi A}{T}\sin(\frac{2\pi}{T}x))^2}\,dx$. Likewise, expressions for the relative densities of second-order, third-order and even n-order structures can also be derived:

$$\overline{\rho}_2 = \frac{(S+2L)t + 4\alpha t(S+L) - 3t^2}{2T(L-A)}, \tag{4}$$

$$\overline{\rho}_3 = \frac{(S+2L)t + 4\alpha t(S+L)(1+2\alpha) - 5t^2}{2T(L-A)}, \tag{5}$$

and

$$\overline{\rho}_n = \frac{(S+2L)t + 4\alpha t(S+L)\frac{(2\alpha)^{n-1}-1}{2\alpha-1} - (2n-1)t^2}{2T(L-A)},\ 0 \le \alpha < \frac{1}{2}. \tag{6}$$

Here, for the sake of illustration, we consider an example with amplitude $A = L/4$ and period $T = 2L$. With these values, the expression for relative density can be reformulated as follows:

$$\overline{\rho}_1 = \frac{t}{3L}\left(\frac{S}{L} + 2 - \frac{t}{L}\right), \tag{7}$$

$$\overline{\rho}_2 = \frac{t}{3L}\left(\frac{S}{L} + 2 - \frac{3t}{L} + 4\alpha\frac{S}{L} + 1\right), \tag{8}$$

and

$$\overline{\rho}_3 = \frac{t}{3L}\left(\frac{S}{L} + 2 - \frac{5t}{L} + 4\alpha(1+2\alpha)t\left(\frac{S}{L} + 1\right)\right). \tag{9}$$

These equations are employed to equate the mass among various orders of auxetic metamaterials.

3. Experiments

We conducted uniaxial tensile experiments on polymer sheets to establish the constitutive relation of the base material. Additionally, we performed compression tests on auxetics to demonstrate their substantial deformation behavior and validate the accuracy of the simulation results. Building on the numerical results, reduction ratios within the transform zone of 0.2 to 0.4 were selected, specifically 1/3, 1/4, and 1/5.

3.1. Fabrication of samples

We designed multi-step auxetic metamaterials and compared them to the original auxetic (OA) metamaterials. Samples were fabricated using selective laser sintering (SLS) technology on a commercial 3D printer (EOS model P110). The base material employed was PA 2200, and the fabrication process utilized a laser power of 30 W and a scanning speed of 5 m/s. The operational temperature was maintained at 190 °C, and the layer thickness was set at 0.06 mm. After manufacturing, an ultrasonic bath was used to remove any unsintered powder residue. Each specimen comprises 5 × 7 unit cells. Six configurations at a relative density of 0.2 were investigated. The design dimensions for third-order auxetic configuration with $\alpha = 1/3$ (T-1/3A) are 200 mm × 186.69 mm × 26.67 mm, whereas for the other configurations they are 150 mm × 140 mm × 20 mm. In the case of equal relative densities, the T-1/3A sample would have extremely thin thicknesses if all the samples had the same dimensions. The limitations of 3D printing technology make it difficult to make samples of this extremely thin thickness, so we chose to scale up the overall size of this sample. At this scale, the geometrically isometric enlargement of the structure has little effect on its mechanical behavior. The values 26.67 mm and 20 mm correspond to the out-of-plane thicknesses of the samples, respectively. The OA configuration has a wall thickness of 1.48 mm. Additionally, five high-order configurations were selected to examine the impact of the inner structure and the hierarchical distribution on mechanical properties. The second-order auxetic configuration with $\alpha = 1/5$ (S-1/5A) has a wall thickness of 0.9 mm. Similarly, other second-order auxetic configurations are abbreviated as S-1/4A ($\alpha = 1/4$) and S-1/3A ($\alpha = 1/3$). Their corresponding wall thicknesses are 0.82 mm and 0.72 mm, respectively. For third-order auxetic configurations, only $\overline{\rho} = 0.2$ is considered here due to the limitation of the inner structure. The wall thicknesses of third-order auxetic configuration with $\alpha = 1/4$ (T-1/4A) and T-1/3A are 0.74 mm and 0.72 mm, respectively. One sample was manufactured for uniaxial compression experiments for each configuration. Detailed geometrical parameters for the fabricated samples are summarized in Table 1. The maximum measured dimensions were within 1% of the designed values, and the maximum mass error between as-designed and measured samples was less than 9.5%.

Table 1
Measured dimensions and mass error of the printed specimens.

Type	Relative density	Direction 1 (mm)	Direction 2 (mm)	Direction 3 (mm)	Error on mass (%)
OA	0.2	149.39	140.46	20.16	3.5
S-1/5A	0.2	149.54	139.52	20.33	−2
S-1/4A	0.2	148.73	140.09	20.01	5
S-1/3A	0.2	149.59	140.77	19.84	9.5
T-1/4A	0.2	148.72	139.13	19.84	1.5
T-1/3A	0.2	198.46	185.47	26.45	0.5

3.2. Characterization of the base material

To obtain the mechanical properties of the base material, we fabricated five dog-bone specimens for tensile testing in accordance with ASTM 638 standards, using the same laser processing method employed for auxetic samples. The stress–strain curves (Fig. 2a) for these specimens were acquired through tensile tests conducted on the printed specimens using a 50 kN universal testing machine (INSTRON-5569) at room temperature, with a constant loading rate of 10^{-3} s^{-1}. The axial tensile strain was measured with a mechanically clamped extensometer. The average Young's modulus is about 1.27 GPa, and the 0.2% offset yield stress is about 25 MPa. The base material did not break suddenly after reaching maximum stress. Instead, it continued to stretch for a period of time before fracturing, exhibiting a softening behavior with a slight decrease in stress. The material fractured at a strain of 0.2, corresponding to a strength of 40.7 MPa.

3.3. Experimental procedure

Compression experiments were conducted using an Instron machine equipped with a 50 kN load cell, operating at a nominal strain rate of 10^{-3} s^{-1}. During the experiment, specimens were centrally positioned on the loading device platen in the front and rear directions to prevent eccentric forces and out-of-plane instability, as shown in Fig. s2. A preload force was applied to avoid slipping between the specimens and platens. The loading continued until the applied strain reached 0.6. An optical camera recorded the deformation process and was used to adjust the load and displacement curves through a digital image correlation algorithm Eberl et al. (2006), which provides sub-pixel resolution for tracking and analyzing displacement. To mitigate boundary effects, Poisson's ratio was calculated from the average longitudinal and transverse strain, measured at four reference points along the central row of auxetics. Similarly, the elastic modulus was calculated based on the longitudinal strain. For tracking the deformation path of the entire structure, one point was marked on the right side of the samples. Engineering stress and strain were determined by dividing the measured force and displacement by the cross-sectional area and height of specimen, respectively.

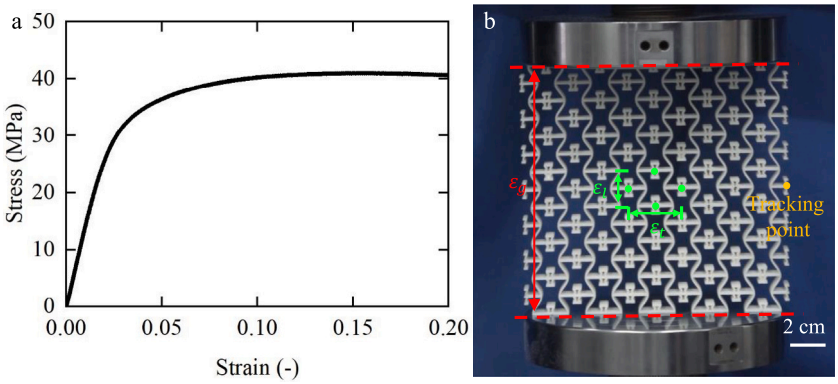

Fig. 2. (a) Measured stress–strain curve of the base material. (b) Definition of reference points and lines for tracking local and global strains in the printed samples during the compression tests.

4. Numerical simulations

To determine the elastic mechanical properties of the first-order, second-order, and third-order auxetic structures, a series of unit cell models were constructed using the commercial software Abaqus. These models covered a range of reduction factors α from 1/5 to 1/3 and relative densities from 0.05 to 0.2. Due to their thin thickness, auxetic structures with low relative densities ($\overline{\rho} = 0.05$) were built using the quadrilateral shell elements (type S4R of the Abaqus element library) following Simpson's rule with 5 integration points across the thickness. For auxetic structures with high relative densities ($\overline{\rho} = 0.1, 0.15, 0.2$), first-order solid elements (type C3D8R) were used, with a minimum of four elements through the thickness. The T-1/4A unit cell has the highest number of mesh elements, approximately $1,746,800$. In all models, the unit cell geometrical dimensions are set to 30 mm × 20 mm × 20 mm. The corresponding wall thicknesses were adjusted with the relative density. We used an isotropic elasto-plastic model with isotropic hardening behavior to represent the mechanical properties of the constituent materials. The specific mechanical parameters are detailed in Fig. 2a, and the material Poisson's ratio is set to 0.4. Periodic boundary conditions are applied to unit cell models by matching mesh nodes on opposite planes with linear constraint equations. Young's modulus and effective Poisson's ratio were determined through elastic simulations with an applied strain of 10^{-4}.

To explore the nonlinear mechanical behaviors of the first-order, second-order, and third-order auxetic structures, we generated numerical models consisting of 5 × 7 unit cells for all considered relative densities. The multi-cell models were meshed using quadrilateral shell elements (S4R type) for a relative density of 0.05, and planar elements (CPS4R type) for the other cases. We chose different elements because simulating the plastic deformation of the array under quasi-static compression with solid elements would require significant computational resources due to the large number of unit cells. After evaluating various approaches, we found that planar elements (CPS4R type) provided sufficient accuracy while improving computational efficiency. The largest numerical model contained approximately 2.2 million mesh elements to ensure mesh accuracy. The numerical model was positioned between two analytical rigid surfaces. The bottom plate was held fixed, while the top plate moved continuously downward to compact the sample by 60%. We defined potential contacts using general contact in explicit dynamic simulations, with contact properties set to hard contact in the forward direction and a tangential friction coefficient of 0.1. The loading velocity was meticulously chosen to ensure that the ratio of kinetic energy to internal energy remains below 1%, allowing us to disregard the influence of loading velocity. The axial stress is used to characterize the collapse strength of each step, either as plateau stress (in stable mode) or peak stress (in unstable mode). The compression modulus is defined by the maximum tangent modulus in each step.

4.1. Large inelastic deformation response to uniaxial compression

Fig. 3 illustrates the stress–strain response of auxetic structures with varying relative densities, as determined through numerical simulations. At a relative density of 0.05, the OA structure undergoes an initial elastic deformation, followed by a weakly nonlinear and progressively increasing behavior. Upon reaching the first peak stress of approximately 6 kPa, the OA structure experiences irreversible global instability, resulting in a weakly nonlinear decreasing response until densification occurs. This dominant mechanism remains consistent for OA with higher relative density. Similar deformation trends and stress–strain responses are evident in Figs. 5a and 3.

Regarding multi-step configurations, the deformation mechanisms and compressive response undergo significant changes influenced by both the inner structure and the relative density. Similarly, all multi-step configurations display an initial elastic behavior followed by a compression response that nearly plateaus, albeit with lower stress levels. As the applied strain progresses, all configurations transition into the second phase, and the stresses exhibit a noticeable trend of stepwise increase.

A larger size of the embedded microstructure leads to an earlier reconfiguration strain and a more stable reconfiguration path. For all relative densities, S-1/3A exhibits no noticeable buckling behavior (See Figs. 4b and 5d). The corresponding reconfigured strain is approximately 0.1. The compression response of these configurations increases gradually but persistently, which we attribute to the contact between the emended structures and the outer structures. In the case of configuration S-1/4A, global buckling occurs prior to the initiation of reconfiguration. However, the rotating mechanism overcomes the buckling mechanism, leading to the reconfiguration of S-1/4A into a stable mode at an applied strain of approximately 0.25 (See Fig. 5c). The deformation is uniform, and the corresponding response remains almost constant. For configuration S-1/5, the game between the two mechanisms mainly depends on the relative density. When the relative density is below 0.1, reconfiguration is primarily influenced by buckling, and the compression response is not significantly enhanced. Conversely, the opposite holds true for high relative density (See Figs. 4a and 5b). The corresponding reconfigured strain is approximately 0.33. Configurations T-1/3A and T-1/4 undergo two reconfigurations during the deformation process (See Fig. 5e and f). Their initial reconfiguration coincides with the strain level observed in their second-order counterparts. Notably, both the deformation process and the associated compression response demonstrate stability in the subsequent stage. The second reconfiguration strains for configurations T-1/3A and T-1/4 are recorded at 0.28 and 0.46, respectively. During the third step, the response of T-1/3A consistently demonstrates a distinctive plateau behavior across all relative density values. In contrast, T-1/4A exhibits either a continuously increasing nonlinear response at low relative density or an escalating nonlinear response followed by a peak stress at high relative density.

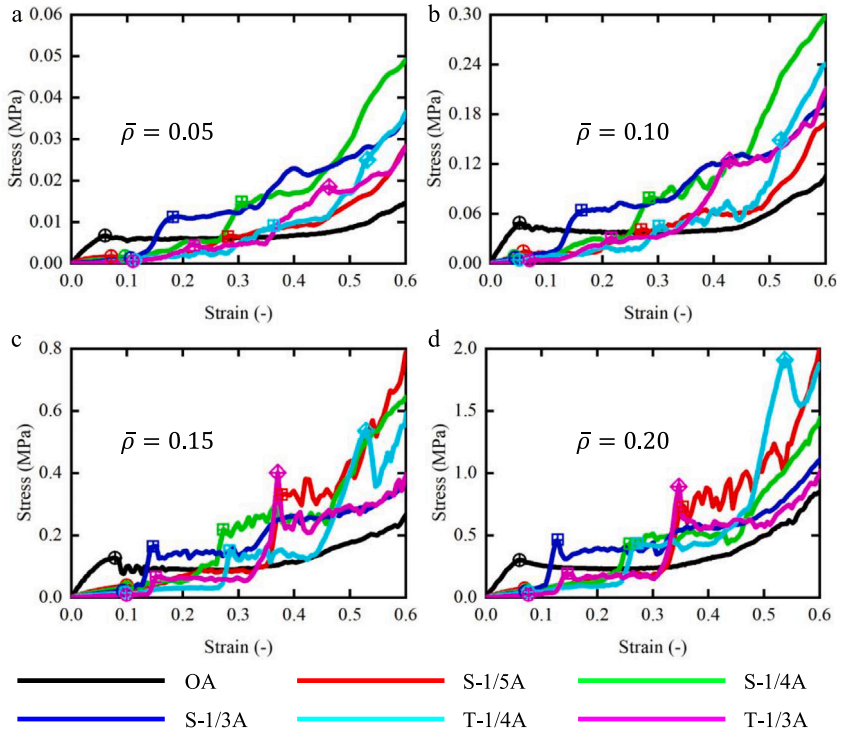

Fig. 3. Nonlinear compressive response of six distinct auxetic configurations across a spectrum of relative densities, ranging from 0.05 to 0.2 at an interval of 0.05. In configuration names S-1/5A, S-1/4A, S-1/3A, T-1/4A, and T-1/3A, the fraction is the value of parameter α.

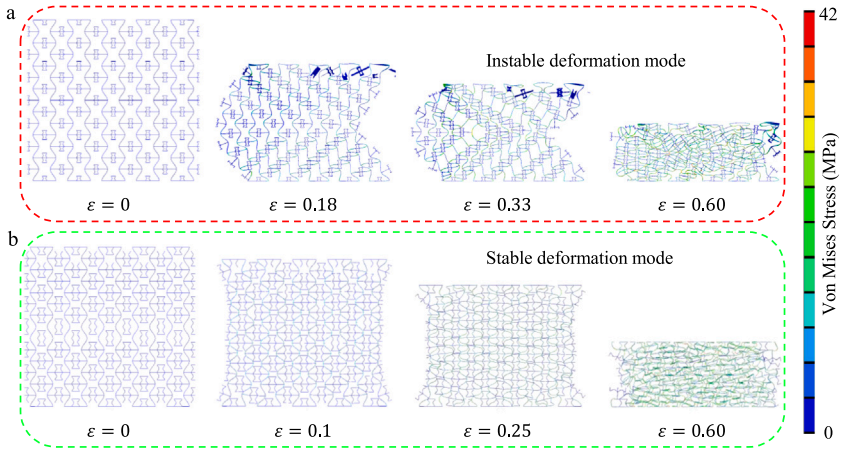

Fig. 4. For relative densities below 0.1, the selected deformed frames for (a) S-1/5A are dominated by an unstable reconfigured mechanism, whereas (b) other multi-step configurations are governed by a stable reconfigured mechanism, with configuration S-1/3A considered in the illustration.

4.2. Effect of embedded structures on compression modulus

Fig. 6a depicts comparison of relative elastic modulus obtained from numerical simulation for all configurations. For all configurations, the relative elastic modulus scale nonlinearly with relative density. The relative elastic modulus of OA and S-1/5A can be approximated by the nonlinear functions

$$E_{\mathrm{OA}}/E_{\mathrm{s}} = (1081\bar{\rho}^3 - 68.01\bar{\rho}^2 + 2.434\bar{\rho})/1000 \tag{10}$$

and

$$E_{\mathrm{S-1/5A}}/E_{\mathrm{s}} = (168\bar{\rho}^3 + 4.567\bar{\rho}^2 - 0.4278\bar{\rho})/1000. \tag{11}$$

The incorporation of embedded structures clearly reduces the elastic modulus of OA. Specifically, the elastic modulus of OA is nearly 4 times larger than that of S-1/5A. Moreover, the expected trend suggests a further decrease in elastic modulus with an increase in the size of the inner structure. Notably, S-1/3A exhibits an elastic modulus comparable to T-1/4A. Furthermore, the elastic modulus of T-1/3A is merely 1/20th of that of OA, which is not easily attained even in bending-dominated structures and auxetics. This phenomenon arises from the observation that the thickness of the multistage structure, featuring distinct embedded microstructures, is smaller than that of the original structure at the same relative density. The ability to tailor the elastic modulus to any value lower than OA by adjusting the embedded structure is readily imaginable.

In Fig. 6b, the variations in the high-order compression modulus for all multi-step auxetics are illustrated, with OA serving as the reference. Notably, it is observed that all high-order compression moduli are significantly higher than their corresponding first-order modulus, which we attribute to the influence of contacts in reconfiguration. After the first reconfiguration, the outermost layer of the unit cell interfaces with

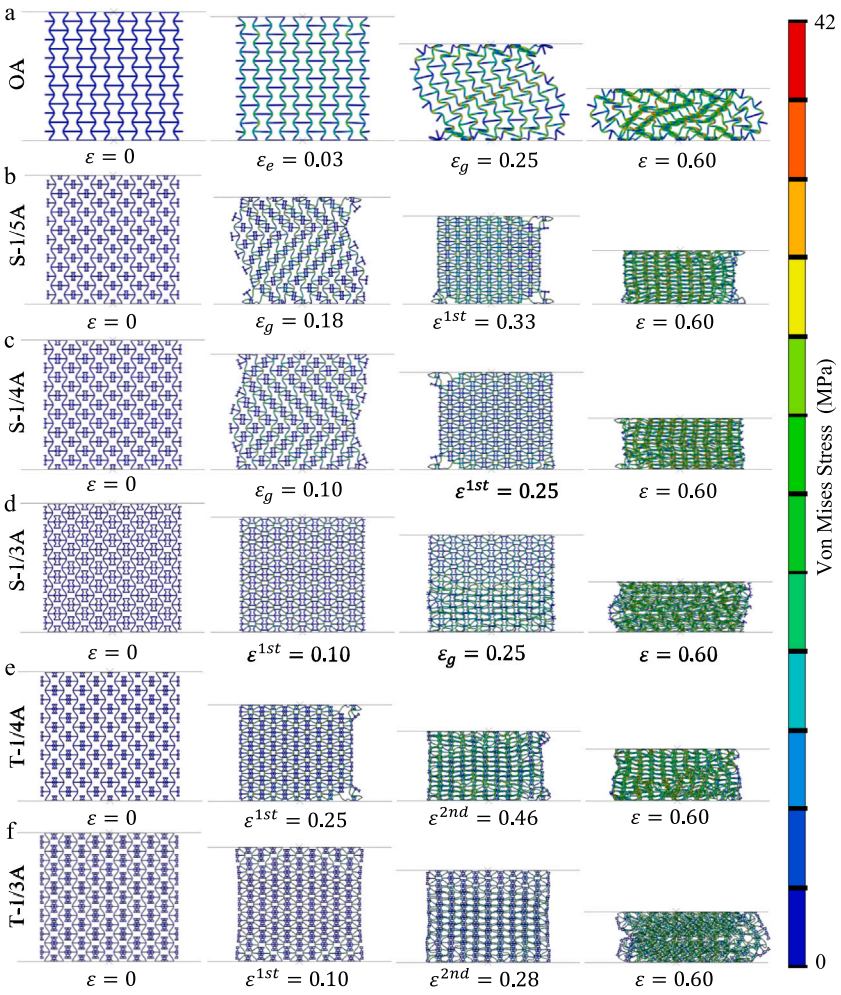

Fig. 5. Large strain simulation results: deformation pattern of auxetic structures with a relative density of 0.2 under compression strains, encompassing stages such as the initial state, elastic deformation, first reconfiguration, second reconfiguration, global buckling, and the final state.

the embedded microstructure, initiating its deformation. Following the second reconfiguration, the embedded microstructures at the top and bottom of the unit cell come into contact with each other. These reconfigurations elevate the embedded microstructure to the primary load-bearing component, reducing the role of the outermost layer. Despite having the same thickness, the embedded microstructure exhibits a higher compressive modulus than the outermost layer, significantly enhancing the overall compressive modulus of the structure and gradually establishing the embedded microstructure as the predominant load-bearing element. Moreover, these increases are closely associated with the deformed stability of these multi-step auxetics and the ability of stretching-dominated reconfiguration to resist deformation. As the relative density drops below 0.1, all configurations exhibit a higher high-order compression modulus than OA, with the exception of S-1/5A and T-1/3A (2-order). S-1/5A is notable for its unstable reconfiguration process, whereas the reconfiguration of T-1/3A is comparatively more flexible than other configurations. At other relative densities, all configurations prove to be stiffer than OA, with T-1/3A (2-order) persisting as the weakest among them. Notably, S-1/5A experiences an increase to about 3.8 times that of OA, which we attribute to the change in deformation stability. T-1/3A (3-order) exhibits the highest stiffness, reaching approximately 4 to 5 times that of OA.

4.3. Effect of embedded structures on compression strength

Fig. 7a illustrates the variations in relative strength across different relative densities for all configurations. Similar to Young's modulus, the first-order relative strength is nonlinear with relative density. The relative compression strength of OA and S-1/5A can also be approximated by the nonlinear functions

$$\sigma_{\mathrm{OA}}/\sigma_{\mathrm{s}} = (1531\bar{\rho}^3 - 43.03\bar{\rho}^2 + 6.958\bar{\rho})/1000 \tag{12}$$

and

$$\sigma_{\mathrm{S-1/5A}}/\sigma_{\mathrm{s}} = (-70.4\bar{\rho}^3 + 104.9\bar{\rho}^2 - 3.767\bar{\rho})/1000. \tag{13}$$

For the same reasons as with Young's modulus, the first-order relative strength decreases with order or scale factor. The relative strength of S-1/5A is nearly a quarter of that of OA. For all relative densities, the ratio of OA to T-1/3A can extend to a significant value of 14.9. This remarkably low strength and stiffness renders it conducive to reusability, even when employed with brittle base materials.

In Fig. 7b, the first-order compression strength of OA is contrasted with the high-order compression strength of other multi-step auxetics. Observations reveal that 3rd order configurations consistently exhibit the lowest strength levels, as they fail to fully utilize every part in the second step. Configuration T-1/3A displays the lowest compression strength, registering absolute values approximately 60% of OA. Concurrently, the compression strength ratio of T-1/4A fluctuates around 1. Configurations S-1/4A and S-1/3 are noted to exhibit a moderate level of compression strength. Notably, the compression strength ratio of S-1/5A hovers around 1 for relative densities below 0.1, but shifts to around 2 for relative densities exceeding 0.1. This serves as additional evidence of the transition of S-1/5A from an unstable to a

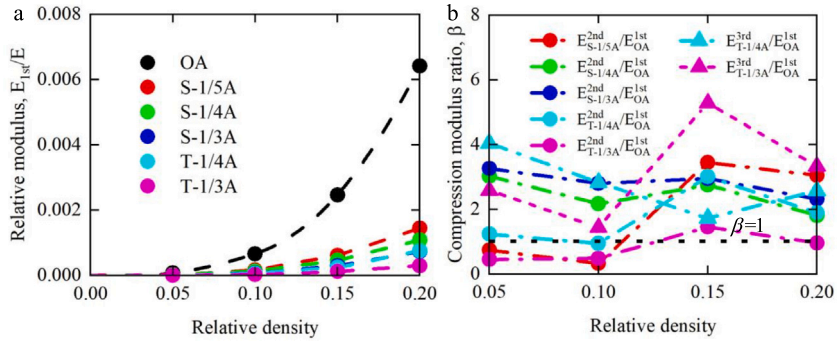

Fig. 6. (a) Variations in the relative Young's modulus across different configurations as a function of relative density evolution. Notably, the elastic modulus of OA surpasses that of other configurations significantly. (b) Relative ratios of high-order compression modulus in multi-step configurations to the Young's modulus of the base OA for selected relative densities. All high-order compression moduli are significantly higher than their corresponding first-order modulus.

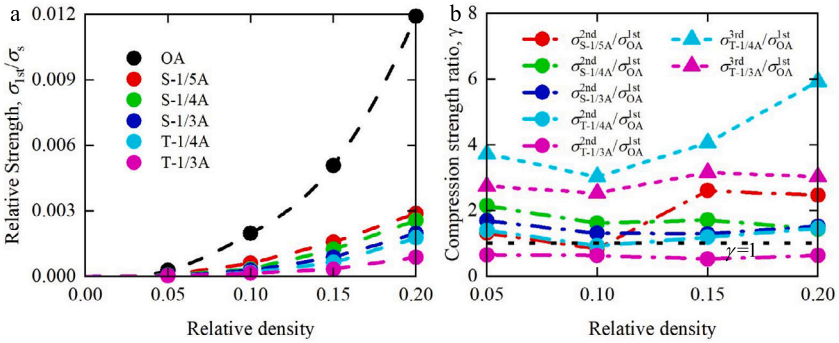

Fig. 7. (a) Evolution of the relative compression strength as a function of relative density, revealing a consistent decrease in first-order relative strength with increasing order or scale factor. (b) Ratios between high-order compression strength of multi-step auxetics and first-order compression strength of OA at specific relative densities. Notably, most configurations exhibit higher high-order compression strength than OA.

stable state. As the deformation advances into the third phase, the 3rd order configurations undergo a reconfiguration to attain the final stage, characterized by an ultra-strong state. Thus T-1/4A exhibits the highest compression strength, reaching approximately 4 to 6 times that of OA.

4.4. Effect of embedded structures on Poisson's ratio

Fig. 8 illustrates the variation of Poisson's ratio with strain, derived from numerical simulations for all configurations at four distinct relative densities. In general, second-order auxetics exhibit nearly the same Poisson's ratios as third-order auxetics, primarily owing to the almost identical thickness of the outer structure. For all relative densities, all configurations exhibit nearly the same initial negative Poisson's ratio values of approximately −1, followed by a consistent and gradually increasing trend. For configurations OA and S-1/5A ($\bar{\rho} \leq 0.1$), the auxetic behavior persists until irreversible global buckling occurs at an applied strain of approximately 0.05. The ultimate Poisson's ratio(the Poisson's ratio of the structure when it is about to destabilize) ranges from −0.87 to −0.65 across different relative densities. In high relative density scenarios, the deformation mode undergoes a substantial transformation in configuration S-1/5A upon the loss of stability.

The contraction of the unit cell slows down and Poisson's ratio experiences a rapid increase, reaching a positive value of either 0.36 or 0.7. Continuing the loading process amplifies the degree of instability, leading to a reversal in Poisson's ratio back to a negative value. At an applied strain of approximately 0.18, the inner structure begins to make contact with the outer structure in an asymmetrical manner, as depicted in Fig. 8d. Subsequently, the structure undergoes reconfiguration, transitioning to another stable stage at a strain of about 0.2. This transition coincides with a rapid decrease in Poisson's ratio, reaching its peak value. Upon reconfiguration, Poisson's ratio undergoes a sudden jump from the peak value to −1. As the applied strain continues to increase thereafter, Poisson's ratio displays a slow and gradual ascent, ultimately reaching 0. The stabilization of Poisson's ratio at approximately 0 is attributed to the occurrence of layer-by-layer collapse. For configurations S-1/4A and T-1/4A, local buckling manifests in a more gradual and subdued manner. Notably, the slopes of their Poisson's curves are evidently smaller compared to configuration S-1/5A. Similarly, configurations S-1/4A and T-1/4A exhibit a comparable yet more moderate jumping behavior compared to configuration S-1/5A. However, it is important to note that the deformation mode for each extreme point remains distinct. In the first two extreme points, the inner structure comes into contact with the outer structure on one side and on two sides, respectively. Reconfiguration is completed at the third extreme point, and the corresponding Poisson's ratio then stabilizes at around 0. For configurations S-1/3A and T-1/3A, their distinctive structural properties effectively suppress the occurrence of both local buckling and global buckling. The resulting deformation in these configurations is uniform, leading to a stable negative Poisson's ratio plateau throughout the reconfiguration process. Until the configurations are reconfigured and undergo layer-by-layer buckling, the Poisson's ratio increases rapidly to 0 and then stabilizes near 0. Consequently, the proposed multi-step mechanism extends the duration of auxetic behavior, providing more opportunities for tailoring mechanical properties.

4.5. Effect of embedded structures on energy absorption

For energy absorbing materials, specific energy absorption (SEA) is typically characterized as the work accomplished through uniaxial compression, consistently evaluated up to a defined strain, here set at 0.6, per gram of mass as

$$\mathrm{SEA} = \frac{V \int_0^{0.6} \sigma d\varepsilon}{M} \tag{14}$$

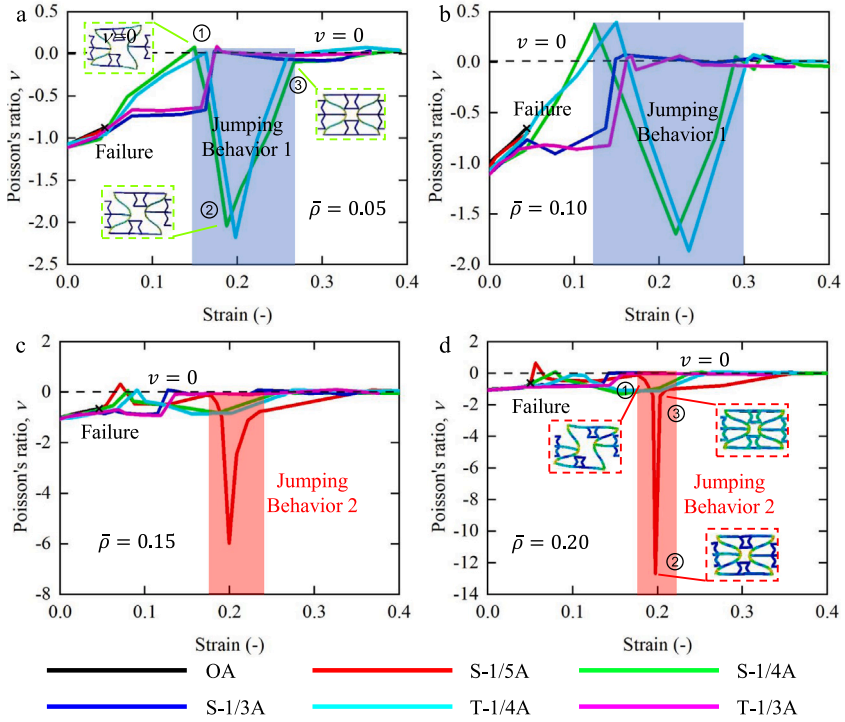

Fig. 8. Evolution of the Poisson's ratios as a function of compressive strain for all relative densities. In the case of configurations OA, the auxetic behavior persists until irreversible global buckling takes place. In contrast, other high-order configurations with jumping behavior span a wide range of auxetic behavior.

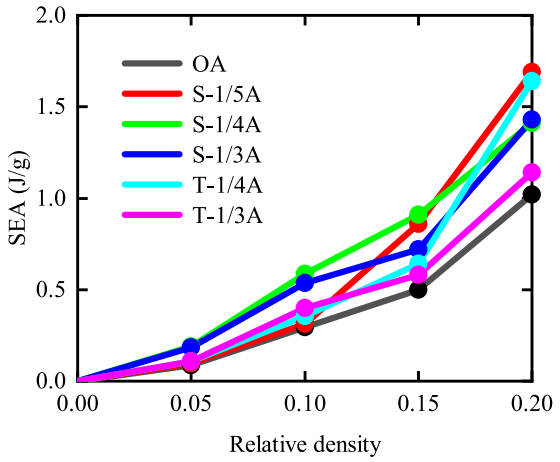

Fig. 9. Evolution of SEA for all configurations as a function of relative density. Multi-step auxetics outperform conventional auxetics for strain energy absorption.

Fig. 9 illustrates the evolution of SEA across diverse configurations with respect to changing relative densities. Notably, it becomes evident that multi-step auxetics exhibit a superior capacity for absorbing strain energy compared to conventional auxetics. When the relative density does not exceed 0.1, configurations S-1/4A and S-1/3A exhibit optimal performance in SEA, surpassing OA by almost 2.1 times. This superiority can be attributed to either a commendably stable nonlinear response or a recoverable buckling mechanism. At this stage, these two deformation mechanisms are mutually compatible. At a relative density of 0.15, S-1/4A processes the highest SEA of about 0.91 J/g. Intriguingly, the energy absorption capacity of S-1/5A shifts from the lowest to the second-best level. Furthermore, at a relative density of 0.2, the SEA value of S-1/5A stands out favorably when compared to other configurations, underscoring the success of the recoverable buckling mechanism. Notably, the energy-absorbing capacity of T-1/4A undergoes a significant enhancement, as anticipated for high relative density.

5. Experimental results and discussion

Fig. 10a showcases the experiment and FEM results of the stress–strain curves of the original and second-order deformation metamaterials. Fig. 10c showcases the deformation frames of the OA structure, featuring main load-bearing components intricately shaped in a sinusoidal manner to mitigate stress concentrations. In the course of compression along the *y* axis (refer to Video S1), the structural deformation can be broadly categorized into three stages: elastic deformation, global instability, and densification. Initially, the structure undergoes overall inward shrinkage, attributed to its inherent negative Poisson's ratio property, constituting a phase of linear elastic deformation. The structure exhibits a linear response with increasing stress during this stage, as depicted in Fig. 10a and b. Upon reaching the initial peak stress of approximately 0.35 MPa, the structure gradually loses stability and protrudes outward to the right side in the mid-plane. Correspondingly, the stress plateaus after a slight decrease. As the deformation progresses further, the structure gradually undergoes densification, accompanied by a slow increase in stress.

Fig. 10d and e present the deformation frames of the second-order auxetic structures S-1/5A and S-1/4A, showcasing behavior distinct from what was observed for OA. Intriguingly, subtle variations in the size of the embedded micro-structures (1/5 and 1/4) result in distinct behavior of the system during deformation, as evidenced in Videos S2 and S3. The deformation process of these structures is broadly characterized into five stages with two distinct steps: elastic deformation, global instability, instability recovery, layer-by-layer buckling, and densification. Initially, the structures experience elastic deformation, with stress gradually increasing until reaching approximately 0.05 MPa. The exceptionally low stress levels observed, unmatched in structures dominated by either bending or stretching with equal relative density, highlight their compelling potential for impact resistance and body protection. Similar to the OA structure, structures S-1/5A and S-1/4A

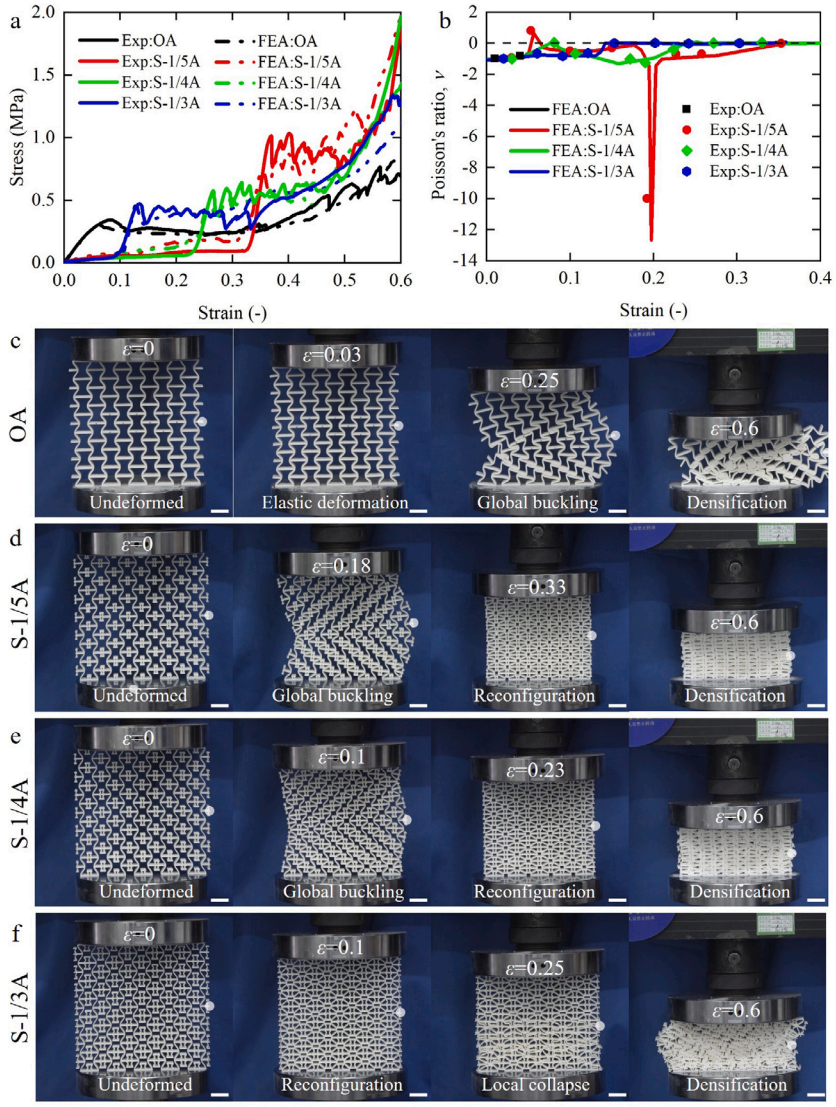

Fig. 10. Compression experiments with auxetics samples fabricated by 3D printing technology. (a) Stress–strain curves and (b) Poisson's ratio for both first-order and second-order auxetics are presented, based on data derived from both experimental observations and simulations. These results, depicted for a relative density of approximately 0.2, demonstrate a close agreement between experimental findings and numerical predictions. (d)–(f) The acquired frames corresponding to compression tests on samples reveal distinct stages, encompassing the initial state, inelastic buckling, subsequent reconfiguration, and the phase of substantial compression up to the maximum applied strain. All scale bars are 2 cm long.

also experience global buckling. The notable difference lies in the recoverability of the instability, stemming from high resistance of the embedded structure to rotating force. This recoverability persists as the applied strain continues, leading to the formation of another stable stage, and the stress value tends to plateau. It becomes evident that the transform strain is primarily determined by the size of the embedded structure: the larger the micro-structure embedded, the smaller the transform strain. Once reconstruction is completed, the stress value increases rapidly, marking the transition into the second step.

After reaching the first peak stress, structures S-1/5A and S-1/4A undergo layer-by-layer collapse in a nearly stable mode, accompanied by small-amplitude oscillations in stress. The first peak of S-1/5A has an amplitude of about 1.01 MPa, nearly twice that of S-1/4A, and almost three times that of OA. This may be attributed to the regenerated stretching-dominated structure making more efficient use of micro-components in terms of loading support. When the applied strain exceeds 0.5, structures S-1/5A and S-1/4A initiate the densification process. Figure 10f presents the deformation frames of the S-1/3A configuration. In contrast to other second-order auxetics, S-1/3A showcases a stable and uniform deformation behavior (See Movie S4) along with an improved second step compression response. Fig. 11 presents stress–strain curves and deformation frames of T-1/4A and T-1/3A (See Movies S5 and S6). In the initial two steps, both configurations exhibit a similar deformation and compression response akin to their lower-order counterpart. With the ongoing applied strain, the second reconstruction occurs through the contact between the third-order inner structure and the second-order inner structure. Ultimately, the stress value decreases, indicative of the overall instability of the structure. For all configurations, both experimental and numerical compressive responses exhibit similar trends. Experimental results are in good agreement with numerical predictions regarding compression modulus, compression, Poisson's ratio, and SEA, as outlined in Table S1. Prediction errors may be attributed to printing errors, imperfections and flaws. For sample T-1/4A, the experimental and simulation results deviate after the second reconfiguration. Quantitative disparities may arise from spatially non-uniform distribution of base materials and geometric imperfections. In numerical simulations, base materials are assumed to have a uniform distribution, yet constrained by current printing technology, their distribution along the thickness tends to be non-uniform. This non-uniformity leads to geometric weaknesses, the

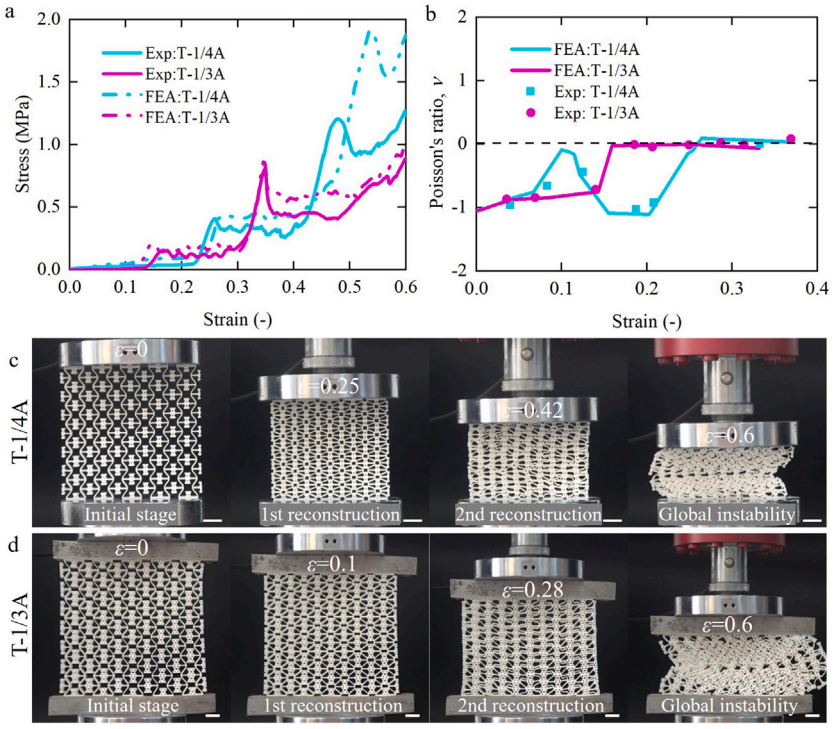

Fig. 11. Uniaxial compression experiments are conducted on T-1/4A and T-1/3A samples with a relative density of 0.2. The results are presented as follows: (a) Engineering stress–strain curves and (b) Poisson's ratio for both T-1/4A and T-1/3A. Notably, simulation results exhibit good agreement with experimental data. Additionally, (c) showcases photographs of the deformed T-1/4A sample during compression, while (d) provides a visual representation of the deformed T-1/3A sample under compression. All scale bars are 2 cm long.

presence of geometric weaknesses causes premature destabilization of the samples during compression tests and thus the experiment results do not reach higher stress levels, which leads to the difference between the experiment results and the FEA results.

To acquire a deeper understanding of the overall instability of the structures, displacements at the right middle position of the structure were individually measured for samples OA, S-1/5A, S-1/4A, and S-1/3A, as illustrated in Fig. 12. In the initial stages of deformation, the labeled positions of all configurations follow the same displacement path, progressing along the negative direction of x owing to the auxetic behavior. When the vertical displacement reaches 5 mm, global buckling becomes dominant in configurations expect for S-1/3A, leading to the labeled points to shift along the positive direction of x. Unlike OA, the labeled points of S-1/5A and S-1/4A move along the negative x direction for the second time when the structure begins to recover from an unstable state to a stable state. Upon reconstruction of the structure, the labeled points cease to move along the x direction and instead move solely along the negative y direction. The integrated microstructure, as a cohesive unit, profoundly shapes the deformation pattern of the system, leading to diverse levels of stable or unstable behavior. In its entirety, the amalgamation of tailored nonlinear response, multi-phase mechanical properties, and augmented energy absorption positions the proposed auxetics as a promising choice for applications in multi-stage load-bearing and impact energy absorption.

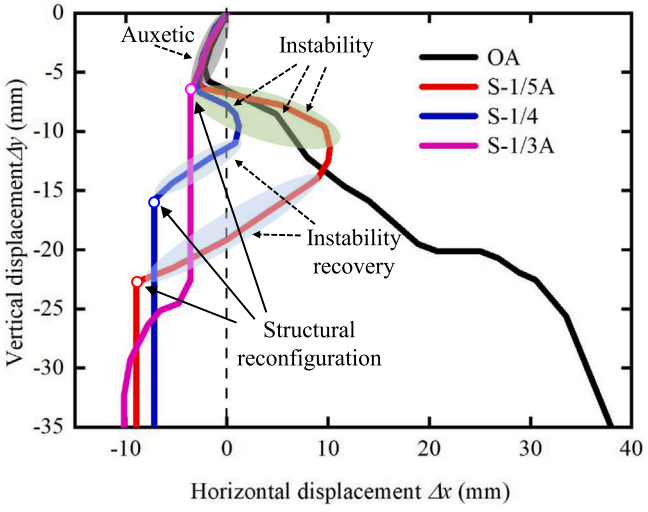

Fig. 12. Displacements at the designated position on the right side of the structure correspond to movement in the positive direction to the right and upward in the horizontal and vertical orientations, respectively.

6. Conclusion

Here, we have presented a novel strategy for designing and fabricating a class of auxetic metamaterial characterized by an extended duration of auxetic behavior, regulated instability, and improved energy absorption. The effective mechanical properties have been investigated both numerically and experimentally. The results demonstrate that the deformation mechanism and compression response of the proposed multi-step auxetics are strongly influenced by the reduction factor and orders of the inner structure. Notably, nonlinear buckling behavior can be completely suppressed when the reduction factor is 1/3. Moreover, we are intrigued to observe that the inclusion of embedded microstructures can restore stable deformation, even in the presence of significant initial instability, particularly with reduction factors of 1/4 and 1/5. Additionally, at a relative density of 0.2, the SEA of sample S-1/5A stands out favorably compared to other configurations, highlighting the success of the recoverable buckling mechanism. Meanwhile, the multi-step auxetics generally exhibit multi-phase compression modulus and strength. Specifically, their low-order modulus and strength are only a

fraction of those of OA, whereas their high-order compression properties are several times greater than those of OA. The exceptional stress levels observed, unmatched in structures dominated by either bending or stretching with equal relative density, highlight their compelling potential for impact resistance and body protection.

CRediT authorship contribution statement

Penghui Yu: Writing – original draft, Software, Methodology, Investigation, Data curation, Conceptualization. **Peijie Zhang:** Validation, Investigation. **Qingxiang Ji:** Validation, Software, Methodology. **Fan Yang:** Validation, Methodology. **Xiaojun Tan:** Writing – review & editing, Validation. **Xueyan Chen:** Writing – review & editing, Writing – original draft, Visualization, Validation, Supervision, Funding acquisition, Conceptualization. **Huifeng Tan:** Writing – review & editing, Supervision, Funding acquisition. **Vincent Laude:** Writing – review & editing, Validation, Conceptualization. **Muamer Kadic:** Writing – review & editing, Supervision, Conceptualization.

Declaration of competing interest

The authors declare that they have no known competing financial interests or personal relationships that could have appeared to influence the work reported in this paper.

Data availability

Data will be made available on request.

Acknowledgments

This work was supported by the National Nature Science Foundation of China under Grant No. 12202118, China Postdoctoral Science Foundation, PR China (2023M730865), Heilongjiang Touyan Team, PR China (HITTY-20190003), Young Elite Scientist Sponsorship Program by Heilongjiang Province, PR China (2022QNTJ0015), Heilongjiang Province Postdoctoral Fund, PR China (LBH-Z22105) and Science Foundation of National Key Laboratory of Science and Technology on Advanced Composites in Special Environments, PR China.

Appendix A. Supplementary data

Supplementary material related to this article can be found online at https://doi.org/10.1016/j.ijsolstr.2024.113040.

References

Babaee, S., Shim, J., Weaver, J.C., Chen, E.R., Patel, N., Bertoldi, K., 2013. 3D soft metamaterials with negative Poisson's ratio. Adv. Mater. 25 (36), 5044–5049.
Berger, J.B., Wadley, H.N.G., McMeeking, R.M., 2017. Mechanical metamaterials at the theoretical limit of isotropic elastic stiffness. Nature 543 (7646), 533–537.
Berinskii, I., 2016. Elastic networks to model auxetic properties of cellular materials. Int. J. Mech. Sci. 115, 481–488.
Bückmann, T., Schittny, R., Thiel, M., Kadic, M., Milton, G.W., Wegener, M., 2014. On three-dimensional dilational elastic metamaterials. New J. Phys. 16 (3), 033032.
Bückmann, T., Stenger, N., Kadic, M., Kaschke, J., Frölich, A., Kennerknecht, T., Eberl, C., Thiel, M., Wegener, M., 2012. Tailored 3D mechanical metamaterials made by dip-in direct-laser-writing optical lithography. Adv. Mater. 24 (20), 2710–2714.
Chen, X., Ji, Q., Iglesias Martinez, J.A., Tan, H., Ulliac, G., Laude, V., Kadic, M., 2022a. Closed tubular mechanical metamaterial as lightweight load-bearing structure and energy absorber. J. Mech. Phys. Solids 167, 104957.
Chen, X., Ji, Q., Wei, J., Tan, H., Yu, J., Zhang, P., Laude, V., Kadic, M., 2020a. Lightweight shell-lattice metamaterials for mechanical shock absorption. Int. J. Mech. Sci. 169, 105288.
Chen, X., Moughames, J., Ji, Q., Iglesias Martínez, J.A., Tan, H., Adrar, S., Laforge, N., Cote, J.-M., Euphrasie, S., Ulliac, G., et al., 2020b. Optimal isotropic, reusable truss lattice material with near-zero Poisson's ratio. Extreme Mech. Lett. 41, 101048.
Chen, X., Moughames, J., Ji, Q., Iglesias Martínez, J.A., Tan, H., Ulliac, G., Laude, V., Kadic, M., 2022b. 3D lightweight mechanical metamaterial with nearly isotropic inelastic large deformation response. J. Mech. Phys. Solids 169, 105057.
Chen, X., Tan, H., 2018. An effective length model for octet lattice. Int. J. Mech. Sci. 140, 279–287.
Cheng, X., Zhang, Y., Ren, X., Han, D., Jiang, W., Zhang, X.G., Luo, H.C., Xie, Y.M., 2022. Design and mechanical characteristics of auxetic metamaterial with tunable stiffness. Int. J. Mech. Sci. 223, 107286.
Choi, J.B., Lakes, R.S., 1996. Fracture toughness of re-entrant foam materials with a negative Poisson's ratio: experiment and analysis. Int. J. Fract. 80, 73–83.
Coulais, C., Sabbadini, A., Vink, F., van Hecke, M., 2018. Multi-step self-guided pathways for shape-changing metamaterials. Nature 561 (7724), 512–515.
Coulais, C., Sounas, D., Alu, A., 2017. Static non-reciprocity in mechanical metamaterials. Nature 542 (7642), 461–464.
Dudek, K.K., Iglesias Martínez, J.A., Ulliac, G., Hirsinger, L., Wang, L., Laude, V., Kadic, M., 2023a. Micro-scale mechanical metamaterial with a controllable transition in the Poisson's ratio and band gap formation. Adv. Mater. 2210993.
Dudek, K.K., Martínez, J.A.I., Ulliac, G., Kadic, M., 2022. Micro-scale auxetic hierarchical mechanical metamaterials for shape morphing. Adv. Mater. 34 (14), 2110115.
Dudek, K.K., Mizzi, L., Iglesias Martínez, J.A., Spaggiari, A., Ulliac, G., Gatt, R., Grima, J.N., Laude, V., Kadic, M., 2023b. Micro-scale graded mechanical metamaterials exhibiting versatile Poisson's ratio. Compos. Struct. 319, 117151.
Eberl, C., Thompson, R., Gianola, D., Bundschuh, S., 2006. Digital image correlation and tracking with Matlab. In: Matlab Central File Exchange.
Evans, K.E., 1991. Auxetic polymers: a new range of materials. Endeavour 15 (4), 170–174.
Evans, K.E., Alderson, A., 2000. Auxetic materials: functional materials and structures from lateral thinking!. Adv. Mater. 12 (9), 617–628.
Evans, K.E., Nkansah, M., Hutchinson, I., 1994. Auxetic foams: modelling negative Poisson's ratios. Acta Metall. Mater. 42 (4), 1289–1294.
Feng, J., Liang, Q., Dou, Y., He, J., Wu, Y., Chen, T., 2022. Higher stiffness hierarchical embedded strengthening honeycomb metastructure with small negative Poisson's ratio reduction. Thin-Walled Struct. 179, 109561.
Florijn, B., Coulais, C., van Hecke, M., 2014. Programmable mechanical metamaterials. Phys. Rev. Lett. 113 (17), 175503.
Frenzel, T., Findeisen, C., Kadic, M., Gumbsch, P., Wegener, M., 2016. Tailored buckling microlattices as reusable light-weight shock absorbers. Adv. Mater. 28 (28), 5865–5870.
Frenzel, T., Kadic, M., Wegener, M., 2017. Three-dimensional mechanical metamaterials with a twist. Science 358 (6366), 1072–1074.
Frenzel, T., Köpfler, J., Jung, E., Kadic, M., Wegener, M., 2019. Ultrasound experiments on acoustical activity in chiral mechanical metamaterials. Nature Commun. 10 (1), 3384.
Gao, W., Kang, J., Wang, G., Ma, H., Chen, X., Kadic, M., Laude, V., Tan, H., Wang, Y., 2023. Programmable and variable-stiffness robotic skins for pneumatic actuation. Adv. Intell. Syst. 2300285.
Gibson, L.J., 2003. Cellular solids. Mrs Bull. 28 (4), 270–274.
Grima, J.N., Alderson, A., Evans, K.E., 2004. Negative Poisson's ratios from rotating rectangles. Cmst 10 (2), 137–145.
Grima, J.N., Evans, K.E., 2000. Auxetic behavior from rotating squares. J. Mater. Sci. Lett. 19, 1563–1565.
Grima, J.N., Evans, K.E., 2006. Auxetic behavior from rotating triangles. J. Mater. Sci. 41 (10), 3193–3196.
Grima, J.N., Gatt, R., 2010. Perforated sheets exhibiting negative Poisson's ratios. Adv. Eng. Mater. 12 (6), 460–464.
Grima, J.N., Jackson, R., Alderson, A., Evans, K.E., 2000. Do zeolites have negative Poisson's ratios? Adv. Mater. 12 (24), 1912–1918.
Grima, J.N., Manicaro, E., Attard, D., 2011. Auxetic behaviour from connected different-sized squares and rectangles. Proc. R. Soc. A 467 (2126), 439–458.
Grima, J.N., Mizzi, L., Azzopardi, K.M., Gatt, R., 2016. Auxetic perforated mechanical metamaterials with randomly oriented cuts. Adv. Mater. 28 (2), 385–389.
Ha, C.S., Plesha, M.E., Lakes, R.S., 2016. Chiral three-dimensional lattices with tunable Poisson's ratio. Smart Mater. Struct. 25 (5), 054005.
Han, S.C., Lee, J.W., Kang, K., 2015. A new type of low density material: Shellular. Adv. Mater. 27 (37), 5506–5511.
Huang, X., Guo, W., Liu, S., Li, Y., Qiu, Y., Fang, H., Yang, G., Zhu, K., Yin, Z., Li, Z., et al., 2022. Flexible mechanical metamaterials enabled electronic skin for real-time detection of unstable grasping in robotic manipulation. Adv. Funct. Mater. 32 (23), 2109109.
Hyatt, L.P., Harne, R.L., 2022. Rapid pneumatic control of bimodal, hierarchical mechanical metamaterials. Adv. Eng. Mater. 24 (7), 2101375.
Jang, D., Meza, L.R., Greer, F., Greer, J.R., 2013. Fabrication and deformation of three-dimensional hollow ceramic nanostructures. Nature Mater. 12 (10), 893–898.
Jiang, B., Chen, X., Yu, J., Zhao, Y., Xie, Z., Tan, H., 2022a. Energy-absorbing properties of thin-walled square tubes filled with hollow spheres. Thin-Walled Struct. 180, 109765.
Jiang, Y., Liu, Z., Matsuhisa, N., Qi, D., Leow, W.R., Yang, H., Yu, J., Chen, G., Liu, Y., Wan, C., et al., 2018. Auxetic mechanical metamaterials to enhance sensitivity of stretchable strain sensors. Adv. Mater. 30 (12), 1706589.
Jiang, H., Ren, Y., Jin, Q., Zhu, G., Hu, Y., Cheng, F., 2020. Crashworthiness of novel concentric auxetic reentrant honeycomb with negative Poisson's ratio biologically inspired by coconut palm. Thin-Walled Struct. 154, 106911.

Jiang, F., Yang, S., Qi, C., Liu, H.-T., 2022b. Two plateau characteristics of re-entrant auxetic honeycomb along concave direction. Thin-Walled Struct. 179, 109665.
Jiang, W., Zhang, X.G., Han, D., Wang, L., Chen, W.Q., Xie, Y.M., Ren, X., 2023. Experimental and numerical analysis of a novel assembled auxetic structure with two-stage programmable mechanical properties. Thin-Walled Struct. 185, 110555.
Lakes, R., 1987. Foam structures with a negative Poisson's ratio. Science 235 (4792), 1038–1040.
Lakes, R., 1991. Deformation mechanisms in negative Poisson's ratio materials: structural aspects. J. Mater. Sci. 26, 2287–2292.
Li, J., Arora, N., Rudykh, S., 2021a. Elastic instabilities, microstructure transformations, and pattern formations in soft materials. Curr. Opin. Solid State Mater. Sci. 25 (2), 100898.
Li, X., Fan, R., Fan, Z., Lu, Y., 2021b. Programmable mechanical metamaterials based on hierarchical rotating structures. Int. J. Solids Struct. 216, 145–155.
Lu, H., Wang, X., Chen, T., 2022. Design and quasi-static responses of a hierarchical negative Poisson's ratio structure with three plateau stages and three-step deformation. Compos. Struct. 291, 115591.
Luo, C., Han, C.Z., Zhang, X.Y., Zhang, X.G., Ren, X., Xie, Y.M., 2021. Design, manufacturing and applications of auxetic tubular structures: A review. Thin-Walled Struct. 163, 107682.
Masters, I., Evans, K., 1996. Models for the elastic deformation of honeycombs. Compos. Struct. 35 (4), 403–422.
Meng, Z., Liu, M., Zhang, Y., Chen, C.Q., 2020. Multi-step deformation mechanical metamaterials. J. Mech. Phys. Solids 144, 104095.
Niknam, H., Akbarzadeh, A., 2018. In-plane and out-of-plane buckling of architected cellular plates: Numerical and experimental study. Compos. Struct. 206, 739–749.
Peng, X.-L., Bargmann, S., 2021. A novel hybrid-honeycomb structure: Enhanced stiffness, tunable auxeticity and negative thermal expansion. Int. J. Mech. Sci. 190, 106021.
Prall, D., Lakes, R., 1997. Properties of a chiral honeycomb with a Poisson's ratio of—1. Int. J. Mech. Sci. 39 (3), 305–314.
Ren, X., Das, R., Tran, P., Ngo, T.D., Xie, Y.M., 2018a. Auxetic metamaterials and structures: a review. Smart Mater. Struct. 27 (2), 023001.
Ren, X., Shen, J., Tran, P., Ngo, T.D., Xie, Y.M., 2018b. Auxetic nail: Design and experimental study. Compos. Struct. 184, 288–298.
Smith, C.W., Grima, J.N., Evans, K., 2000. A novel mechanism for generating auxetic behaviour in reticulated foams: missing rib foam model. Acta Mater. 48 (17), 4349–4356.
Tancogne-Dejean, T., Diamantopoulou, M., Gorji, M.B., Bonatti, C., Mohr, D., 2018. 3D plate-lattices: an emerging class of low-density metamaterial exhibiting optimal isotropic stiffness. Adv. Mater. 30 (45), 1803334.
Viard, A.-E., Dirrenberger, J., Forest, S., 2020. Propagating material instabilities in planar architectured materials. Int. J. Solids Struct. 202, 532–551.
Vocke, III, R.D., Kothera, C.S., Woods, B.K., Wereley, N.M., 2011. Development and testing of a span-extending morphing wing. J. Intell. Mater. Syst. Struct. 22 (9), 879–890.
Wagner, M.A., Lumpe, T.S., Chen, T., Shea, K., 2019. Programmable, active lattice structures: Unifying stretch-dominated and bending-dominated topologies. Extreme Mech. Lett. 29, 100461.
Wang, X.-T., Li, X.-W., Ma, L., 2016. Interlocking assembled 3D auxetic cellular structures. Mater. Des. 99, 467–476.
Wang, L., Ulliac, G., Wang, B., Iglesias Martínez, J.A., Dudek, K.K., Laude, V., Kadic, M., 2022. 3D auxetic metamaterials with elastically-stable continuous phase transition. Adv. Sci. 9 (34), 2204721.
Wang, X.-T., Wang, B., Li, X.-W., Ma, L., 2017. Mechanical properties of 3D re-entrant auxetic cellular structures. Int. J. Mech. Sci. 131, 396–407.
Wang, X.-T., Wang, B., Wen, Z.-H., Ma, L., 2018. Fabrication and mechanical properties of CFRP composite three-dimensional double-arrow-head auxetic structures. Compos. Sci. Technol. 164, 92–102.
Wu, W., Liu, P., Kang, Z., 2021. A novel mechanical metamaterial with simultaneous stretching-and compression-expanding property. Mater. Des. 208, 109930.
Xu, F., Yu, K., Hua, L., 2021. In-plane dynamic response and multi-objective optimization of negative Poisson's ratio (NPR) honeycomb structures with sinusoidal curve. Compos. Struct. 269, 114018.
Yang, H., Ma, L., 2020a. 1D to 3D multi-stable architected materials with zero Poisson's ratio and controllable thermal expansion. Mater. Des. 188, 108430.
Yang, H., Ma, L., 2020b. Design and characterization of axisymmetric auxetic metamaterials. Compos. Struct. 249, 112560.
Yuan, S., Shen, F., Bai, J., Chua, C.K., Wei, J., Zhou, K., 2017. 3D soft auxetic lattice structures fabricated by selective laser sintering: TPU powder evaluation and process optimization. Mater. Des. 120, 317–327.
Zhang, J., Lu, G., Ruan, D., Wang, Z., 2018. Tensile behavior of an auxetic structure: Analytical modeling and finite element analysis. Int. J. Mech. Sci. 136, 143–154.
Zhang, X.Y., Ren, X., Zhang, Y., Xie, Y.M., 2022. A novel auxetic metamaterial with enhanced mechanical properties and tunable auxeticity. Thin-Walled Struct. 174, 109162.
Zhang, P., Yu, P., Zhang, R., Chen, X., Tan, H., 2023. Grid octet truss lattice materials for energy absorption. Int. J. Mech. Sci. 259, 108616.
Zheng, X., Lee, H., Weisgraber, T.H., Shusteff, M., DeOtte, J., Duoss, E.B., Kuntz, J.D., Biener, M.M., Ge, Q., Jackson, J.A., et al., 2014. Ultralight, ultrastiff mechanical metamaterials. Science 344 (6190), 1373–1377.
Zhu, S., Tan, X., Wang, B., Chen, S., Hu, J., Ma, L., Wu, L., 2019. Bio-inspired multistable metamaterials with reusable large deformation and ultra-high mechanical performance. Extreme Mech. Lett. 32, 100548.